Fluorescence “Turn-Off” Sensing of Iron (III) Ions Utilizing Pyrazoline Based Sensor: Experimental and Computational Study

Promila Sharma
Punjabi University
Shikha Bhogal
Punjabi University
Irshad Mohiuddin
Punjabi University
Mohamad Yusuf
Punjabi University
Ashok Kumar Malik (malik_chem2002@yahoo.co.uk)
Punjabi University

Research Article

Keywords: Chalcone, Pyrazoline, Fluorescence quenching, iron, DFT

Posted Date: June 24th, 2022

DOI: https://doi.org/10.21203/rs.3.rs-1752598/v1

Abstract

A simple pyrazoline-based "turn off" fluorescent sensor 5-(4-methoxyphenyl)-3-(5-methylfuran-2-yl)-1-phenyl-4,5-dihydro-1*H*-pyrazole (PFM) was synthesized and well characterized by different techniques such as FT-IR, ^{1}H-NMR, ^{13}C-NMR, and mass spectrometry. The synthesized sensor PFM was utilized for the detection of Fe^{3+} ions. Fluorescence emission selectively quenched by Fe^{3+} ions compared to other metal ions (Mn^{2+}, Al^{3+}, Fe^{2+}, Hg^{2+}, Cu^{2+}, Co^{2+}, Ni^{2+}, Cd^{2+}, Pb^{2+}, and Zn^{2+}) via paramagnetic fluorescence quenching and showed good anti-interference ability over the existence of other tested metals. Under optimum conditions, the fluorescence intensity of sensor quenched by Fe^{3+} in the range of 0 to 3 μM with detection limit of 0.12 μM. Binding of Fe^{3+} ions to PFM solution was studied by fluorescent titration, revealed formation of 1:1 PFM-Fe metal complex and binding constant of complex was found to be of 1.3×10^5 M^{-1}. Further, the fluorescent sensor has been potentially used for the detection of Fe^{3+} in environmental samples (river water, tap water, and sewage waste water) with satisfactory recovery values of 99-101%.

Highlights

- The PFM exhibits high selectivity and sensitivity towards Fe^{3+} ions over other different metal ions.
- PFM was utilized for the detection of Fe^{3+} in different water samples (tap, river, and sewage waste water).
- The sensing abilities of PFM towards Fe^{3+} ions was successfully demonstrated by DFT calculations

1. Introduction

Iron, as one of the most fundamental trace element, is known for cell formation in the human body system and growth in plants. Ferric ions (Fe^{3+}) play an imperative role in lots of critical biological processes (e.g. oxygen transfer in haemoglobin, electron-proton transfer, RNA and DNA synthesis, nerve conduction, enzyme synthesis, and regulation of acid-base balance) [1, 2]. However, excess deposition of iron in the human body can cause some severe diseases including hemochromatosis, Parkinson's and Alzheimer's disease, and diabetes [3]. Moreover, the lack of iron in the human body decreases immunity throughout the developmental periods. Subsequently, a trace level of iron plays a vital role in the health of the living organism. Considering importance of evaluation of Fe^{3+} ions concentration, WHO and European legislation have set the permissible limit of iron in drinking water and food as 0.3 ppm (~ 5.4 μM) and 0.2 ppm (~ 3.8 μM) respectively [4]. Thus, quantitative detection of Fe^{3+} ion at an ultra-trace level in environmental samples is of prominent concern using efficient analytical methods. Numerous methods (e.g. atomic absorption spectrometry, spectrophotometry, colorimetry, high-performance liquid chromatography, inductively coupled plasma optical emission spectrometry, and electrochemical analysis) for the detection of Fe^{3+} ions have been used with good aspects [5, 6]. However, all these methods emerged with various limitations such as complicated technologies, sophisticated handling, expensive devices, and a long time for operating systems. Therefore, compared with these methods, the fluorescence sensing strategy has gained considerable attention, as it has protruded optimistic method for monitoring and detection of diverse ions in environmental, and biological samples [7]. This consideration is due to a lot of highlights like simplicity, cost-effectiveness, rapid responses, high selectivity, and sensitivity.

Pyrazolines derivatives, as the most recent fluorescent sensor have generated much excitement because of their multipurpose applicability in various fields compared with other fluorescent emitters [8, 9].The synthetic versatility and the extended synthesis potential of pyrazoline with intrinsic biological and pharmacological activity (e.g. antimalarial, antifungal, anti-inflammatory, antibacterial) have made pyrazoline and its derivatives as one of the most well-known precursors to chemistry [10, 11]. Specifically, the assurance of spectroscopic properties of pyrazoline dyes widely used as pH sensors, metal ion fluorescent sensor, living cell imaging probes, and logic-based devices is of great importance [12, 13].

In this context, and in continuation of our research on pyrazoline based fluorescent sensors [14], we synthesized and characterized a “turn Off” fluorescent chemosensor, namely, 5-(4-methoxyphenyl)-3-(5-methylfuran-2-yl)-1-phenyl-4,5-dihydro-1*H*-pyrazole (PFM). This molecule, detects Fe^{3+} via the paramagnetic enhanced quenching mechanism and offers several advantages such as easy synthesis, high sensitivity and selectivity, and rapid fluorescence quenching response to Fe^{3+} over other metal cations (Al^{3+}, Fe^{3+}, Fe^{2+}, Mn^{2+}, Cu^{2+}, Co^{2+}, Hg^{2+}, Ni^{2+}, Cd^{2+}, Pb^{2+}, and Zn^{2+}). Besides, the DFT calculations were used to confirm the experimental results.

2. Experimental

2.1. Reagents and measurements

All the metal salts and 4-methoxybenzaldehyde were purchased from Loba Chemie Pvt. Ltd. (Mumbai, India). 2-acetyl-5-methylfuran and phenyl-hydrazine were purchased from Sigma-Aldrich (Mumbai, India). The synthesized compounds were characterized by FT-IR, ^{1}H-NMR, ^{13}C-NMR, and mass spectrometry. FT-IR spectra were scanned on a Perkin Elmer Spectrum Infrared Spectrophotometer Version (10.6.0), Japan. ^{1}H-NMR and ^{13}C-NMR spectra were recorded on a 500 MHz Bruker spectrometer, Switzerland. LC-MS Spectrometer Model Q-ToF Micro Waters was used to record the mass spectrum of the PFM. To record absorption spectra of the compounds, UV-1800 Shimadzu UV-Visible spectrophotometer (Shimadzu, Japan) was used. All fluorescence experiments were performed with a Shimadzu RF-5301PC spectrophotofluorometer, (Shimadzu, Japan). Triply distilled water (TDW) was used for the experimental work.

2.2. Synthesis and Characterization of 5-(4-methoxyphenyl)-3-(5-methylfuran-2-yl)-1-phenyl-4,5-dihydro-1*H*-pyrazole (PFM)

The synthesis of pyrazoline derivative PFM is presented in Scheme 1. The starting material chalcone (CFM) was synthesized from 2-acetyl-5-methylfuran and 4-methoxybenzaldehyde as reported in the literature [15]. Then, a mixture of chalcone CFM (2.42 g, 0.01 mol), phenylhydrazine (1.5 g, 0.01mol), KOH (0.5 g, 0.01 mol), and ethanol (20.0 ml) was refluxed continuously for 6 hours and reaction progress was monitored by TLC. After reaction completion, the resulting mixture was neutralized with iced-HCl to yield a dark brown solid mass. Then, the product PFM was recrystallized from MeOH [16].

Dark Brown solid; Yield: 72%; m.p. 179-180^{0}C; FT-IR: υ_{max} (cm^{-1}): 3100 (aromatic C-H) & 1595 (C = N); ^{1}H-NMR (500 MHz, $CDCl_3$): δ 7.17 (4H, m), 7.03 (2H, m), 6.80 (2H, d), 6.73 (1H, d), 6.37 (1H, d), 6.00 (1H, d), 5.11(1H, dd, J_{XM}=12 Hz, J_{XA}=7 Hz, H-X), 3.74(3H, s, 1'-OCH_3), 3.66 (1H, dd, J_{MX}=12 Hz, J_{MA}=17 Hz, H-M), 2.97 (1H, dd, J_{AX}=7 Hz, J_{AM}=17.0 Hz, H-A), 2.33 (3H, s, 1″-CH_3); ^{13}C-NMR (125MHz, CDCl$_3$): δ 159.04,153.86, 146.63, 144.85, 139.36, 134.40, 128.89, 127.12, 119.04, 114.53, 113.58, 111.013, 107.96, 63.4, 55.27, 43.27, 13.91; Calculated ESI-MS: m/z 332.39 for $C_{21}H_{20}N_2O_3$.

2.3. Analytical procedure

Stock solutions (1 μM) of metal salts i.e. Al^{3+}, Fe^{3+}, Fe^{2+}, Mn^{2+}, Cu^{2+}, Co^{2+}, Hg^{2+}, Ni^{2+}, Cd^{2+}, Pb^{2+}, and Zn^{2+} were prepared in triply distilled water. The stock solution of probe PFM (2×10^{-5} M) in methanol: water (1:9, v/v) was prepared.

Investigated the fluorescent behavior of the sensor PFM, the fluorescence excitation and emission wavelength was found to be 350 nm and 484 nm respectively. Afterwards, for selectivity, the fluorescence spectrum of PFM in the presence of each metal salt was recorded. For the fluorescence experiment, 100 μL of PFM solution, 100 μL of metal salt was taken in cuvette and then diluted up to 3ml with triply distilled water. For the better considerations of the quenching behavior of sensor PFM, fluorescence titration was performed in the presence of different concentrations of Fe^{3+} ions (0–3 μM). The limit of detection (LOD) value was obtained from the 3σ/K (where σ is the standard deviation of the blank solution and K represents the slope of the calibration curve between fluorescent intensity and the Fe^{3+} concentrations).

2.4. Binding Measurement's

Job's plot analysis was carried out to identify the binding stoichiometry between sensor PFM and Fe^{3+} ions. The solution of sensor PFM and Fe^{3+} ions were prepared to carry out Job's plot experiments. The plot was constructed from the emission profile by maintaining the sum of the concentration of Fe^{3+} ions and the PFM constant. The fluorescence spectrum was recorded by varying the mole fraction of PFM and Fe^{3+} ions at an excitation wavelength of 350 nm. The emission intensity was plotted against the mole fraction of the Fe^{3+} ions. The molar ratio corresponding to the highest point or inflection point on the Job's plot gives the coordination ratio of the PFM to the Fe^{3+} ions [17]. The association constant of PFM with Fe^{3+} was calculated according to the fluorescence emission intensity data using the modified Benesi–Hildebrand equation:

$$\frac{F_{min} - F_0}{F - F_0} = \frac{1}{K_a[M]} + 1$$

Where, F_0, F, and F_{min} are the fluorescence intensities of PFM in the absence of Fe^{3+} ions, at an intermediate concentration of Fe^{3+} ions, and a concentration of complete interaction of Fe^{3+} ions, respectively. K_a is the association constant and [M] represents the concentration of the metal ion (Fe^{3+}) [1, 18].

2.5. Computational Study

To gain insight into the structures and fluorescence properties of PFM, before and after the addition of metals, density functional theory (DFT) computations were performed on B3LYP/6-311G(d,p)/LANL2DZ using Gaussian 09 software. The optimized geometrical parameters, net charges on active centres, and energetic of the ground state for intermediate chalcone CFM, the sensor (PFM), and its binding with iron metal (PFM-Fe) were calculated. The spectral theoretical results of vibration analysis, ^{13}C-NMR, and ^{1}H-NMR of the ligand molecule were also examined.

2.6. Detection of iron in water samples

Different water samples (river water, tap water, and sewage waste water) were used for the practical applicability of synthesized sensor. The river water was collected from the Ghaggar River (Patiala, Punjab, India). The tap water was collected from the chemistry lab (Khalsa College, Patiala) and sewage waste water was taken from the Punjabi University, Patiala (Punjab, India). All the water samples were filtered through a Grade 1 Whatman filter paper (pore size: 11 μm) and nylon-6,6 membrane filter (0.2 μm per 47 mm) before analysis. All the samples were tested with the proposed method before spiking.

3. Results And Discussion

3.1. Synthesis and Structural Characterizations

The absence of stretching frequency of α, β-unsaturated carbonyl group and the presence of (C = N) and (C-N) stretching frequencies at 1595 cm^{-1} and 1244 cm^{-1} in the IR-spectrum (Figure S1 and S2) of the sensor PFM confirmed the subsequent cyclization of chalcone to form the pyrazoline derivative PFM [19]. In the 500 MHz instruments, the ^{1}H-NMR coupling constant analysis of compound CFM indicated that hydrogen atoms of the olefinic carbon-carbon bond were in a *trans* arrangement (J = 15 Hz) (Figure S3). ^{1}H-NMR spectra of the compound PFM exhibit the presence of two non-equivalent protons of a methylene group (H_A / H_M) at 2.97 ppm and 3.64 ppm, because of the (H-X) proton at vicinal asymmetric carbon. The methene proton (H-X) appeared as a doublet of doublets at 5.11 ppm, because of vicinal coupling with the two magnetically non-equivalent protons of the methylene group at position 4 of the pyrazoline ring (Figure S4) [19]. The carbonyl carbon of the chalcone CFM appeared at 177.39 ppm (Figure S5). A signal due to C = N carbon of the pyrazoline ring was observed in PFM at 159.04 ppm. C4 and C5 carbons of the pyrazoline ring resonated at 63.41 ppm and 43.27 ppm respectively (Figure S6)

[20]. The characteristic peaks of masses were observed at *m/z* 243.44 (Figure S7) and *m/z* 332.39 in the mass spectra of chalcone CFM and ligand PFM (Figure S8).

3.2. Fluorescence and Absorption experiments of PFM for the sensing of Fe^{3+} ion

Different excitation wavelengths (320–400 nm) were optimized to get the maximum fluorescence emission intensity for PFM. The maximum fluorescence emission intensity (484 nm) was observed at excitation wavelength of 350 nm (Figure S9). The selective recognition of different metal ions having concentration 1μM (Al^{3+}, Fe^{3+}, Fe^{2+}, Mn^{2+}, Cu^{2+}, Co^{2+}, Hg^{2+}, Ni^{2+}, Cd^{2+}, Pb^{2+}, and Zn^{2+}) was examined (λ_{ex}-350 nm; λ_{em}- 484 nm). For the selectivity experiment, 100 μL of different metal solution and 100 μL of PFM were taken and diluted to 3mL with TDW. The solution was stirred for 3 minutes and kept undisturbed at room temperature for 15 minutes. A large decrease in fluorescence intensity was observed for Fe^{3+} comparative to other metal cations, showing a selective recognition of Fe^{3+} ion by pyrazoline-based ligand PFM (Fig. 1).

Further, the UV-Vis spectrum of PFM before and after addition of iron (PFM-Fe) was performed (Fig. 2). For PFM, the absorption bands was observed at 286 nm and 366 nm, due to n−π* transitions. The n−π* transition may be due to conjugation between a lone pair electron of the nitrogen atom in the pyrazoline moiety and the π−bond of the benzene ring. Upon addition of Fe^{3+} to the solution containing PFM, the band observed at 286 nm diminished while the absorption of the band at 368 nm is enhanced with a bathochromic shift (363 nm to 378 nm). The changes in band position and intensity is due to an intramolecular charge transfer (ICT) of the sensor PFM due to extended electron conjugation resulting from the binding of Fe^{3+} ion [21].

3.3. Sensitivity study of PFM for Fe^{3+} ion

To quantify the sensitivity and fluorescence quenching behavior between PFM and Fe^{3+}, the sensing proficiency of PFM towards Fe^{3+} was further explored in the range of0-3 μM. On the addition of Fe^{3+} ions in a sequential manner in the PFM solution, the fluorescence emission intensity of the sensor PFM gradually decreases with the increase in concentration of Fe^{3+} (Fig. 3a). The emission intensity of sensor PFM was specifically quenched by Fe^{3+} ions via paramagnetic fluorescence quenching [7, 22]. The quenching phenomena were further analyzed by the Stern-Volmer equation:

$$\frac{F_O}{F} = 1 + K_{sv}\left[Fe^{3+}\right]$$

Where, F_0 is the initial fluorescence intensity of the PFM solution in the absence of Fe^{3+}, F is the fluorescence emission intensity in the presence of Fe^{3+}, and K_{SV} is the Stern-Volmer constant. The Stern-Volmer plot (F_0/F versus [Fe^{3+}]) depicts that the quenching ratio increase linearly with the increase in Fe^{3+}

concentration (R^2 = 0.99) (Fig. 3b). The K_{SV} was calculated from the slope of plot and found to be 4.45 x 10^{-5} M.

The limit of detection (LOD) was calculated 0.12 μM for Fe^{3+} using the equation LOD = 3σ/K, which are far lower than most extreme toxin levels for Fe^{3+} (5.4 μM) in drinking water given by EPA guidelines (Fig. 3c) [4].

3.4. Competitive selectivity of PFM for Fe^{3+} ions

To investigate the selectivity and efficiency of PFM towards Fe^{3+} ions, competitive experiment was carried out. For the competitive study, 1mL of Fe^{3+} (1 μM) was added to the 100 μL of PFM (2 x 10^{-5} M) solution containing other metal ions (Al^{3+}, Fe^{2+}, Mn^{2+}, Cu^{2+}, Co^{2+}, Hg^{2+}, Ni^{2+}, Cd^{2+}, Pb^{2+}, and Zn^{2+} at concentration of 2 x 10^{-6} M) were taken and the fluorescence emission spectra was obtained. The interfering metal ions induced no significant changes in the fluorescence intensity of the sensor PFM (Fig. 4). As a result, the PFM can be presented as a highly selective and reliable fluorescent sensor for Fe^{3+} ion recognition. Moreover, relative error (%) for various metal ions was calculated:

Relative error (%) = $[(F-F_0)/F_0]$ X 100%

where, F_0 and F are the fluorescence emission intensities in the absence and presence of interfering ion. Table 1 validated the relative error (%) values showing great tolerance of other metals over the Fe^{3+} ion. The relative error is also found to be less than ± 5. These results suggest that the metal binding of PFM shows an evident preference for ferric ions over other competing ions.

Table 1
Relative error showing tolerance of other metals

Interferent ion	Relative Error % ($\Delta F/F_0$ x100)
Zn^{2+}	1.411
Hg^{2+}	-1.411
Cd^{2+}	-1.376
Fe^{2+}	0.882
Mn^{2+}	4.4107
Co^{2+}	2.681
Cu^{2+}	-3.0345
Ni^{2+}	-3.493
Pb^{2+}	4.234
Al^{3+}	4.869

3.5. Proposed Binding and Sensing Mechanism

A Job's Plot was performed to calculate the binding stoichiometry of PFM and Fe^{3+} ion (Fig. 5). A turning point at 0.5 mole fractions indicates 1:1 metal-ligand binding interactions between sensor PFM and Fe^{3+}. The association constant (K_a) was calculated to be 1.3 x 10^5 M^{-1} according to the modified Benesi–Hildebrand equation (Fig. 6).

The mechanism of interaction between the Fe^{3+} and PFM was studied through FT-IR (Figure S10). It can be proposed that the formation of the coordination between Fe^{3+} and sensor PFM resulted from electronegative atom nitrogen of the pyrazoline ring and the oxygen of the furyl ring (Fig. 7). This interaction causes the fluorescence quenching of the sensor PFM. The FTIR spectrum of PFM exhibits a peak at 1595 cm^{-1} (stretching vibration C = N), and peak at 1245 cm^{-1} (C-O stretching vibration). However, in the PFM-Fe complex, the characteristic stretching vibration C-O peak of PFM partially disappear while the C = N stretching vibration of pyrazoline ring shifted from to 1595 cm^{-1} to 1561 cm^{-1}. This can be due to the interaction of Fe^{3+} ions with the nitrogen and oxygen atom of PFM. The binding of Fe^{3+} to PFM resulted in the electron or energy transfer from PFM to Fe^{3+} metal ion causes fluorescence quenching of PFM. The fluorescence emission spectra of PFM overlaps with the absorption spectra of Fe^{3+}, suggesting the fluorescence resonance energy transfer (FRET) mechanism for the fluorescence quenching (Figure S11).

3.6. Computational Study

3.6.1. Molecular Geometry optimization

The optimized structures of these compounds along with the labeling of atoms are shown in Fig. 8. After optimization, the binding energies ($\Delta E = E(complex)-E(PFM)$) were calculated for all metals with PFM to obtain the most strong binding of the metal cation with PFM. The calculated result, $\triangle E = -564\ kcalmol^{-1}$ showed the minimum energy changes for iron complex as compared to other metals (Table S1). Also, more negative energy value (-1194.45 a.u.) of the PFM-Fe than the free ligand (-1072.42 a.u.) confirms the stability of the PFM-Fe system compared to other metals showing high selectivity towards iron ions [7, 23, 24].

Also, for chalcone CFM, ligand PFM, and ligand complex (PFM-Fe^{3+}) with iron metal, C–C bond distances are found to be in the range from 1.528–1.533 Ǻ, 1.529–1.539 Ǻ, and 1.531–1.546 Ǻ while for C-N, these values are 1.469 Ǻ, 1.470 Ǻ, and 1.478 Ǻ respectively. In the case of C-H bond distances, they lie in the range from 1.093–1.103 Ǻ, 1.093–1.101 Ǻ, and 1.092–1.098 Ǻ respectively [23].

3.6.2 Mulliken population analysis and Molecular Electrostatic Potential

The Mulliken population analysis is correlated to the vibrational properties and nature of chemical bonds present in the molecule. The Mulliken charge distribution structure and horizontal bar diagram of comparative mulliken atomic charges of the title compounds are shown in Fig. 9a and 9b, respectively. All the hydrogen atoms in the compounds carry a net positive charge. The atomic charge distribution shows that the hydrogen atoms of the methoxy group have a bigger positive atomic charge (0.2e to 0.32e) than the other hydrogen atoms. As expected, the charge of the nitrogen atom (N31= -0.1826, -0.2933 and N32= -0.2574, -0.2008 in PFM and PFM-Fe respectively) is negative. Additionally, the results illustrate that the charge of the oxygen atoms in the carbonyl group of CFM and furyl ring exhibits a negative charge, which acts as donor atoms. The oxygen atom of -OCH_3 group enforces a large negative charge on the carbon (C11= -0.1285, C26= -0.3822, C26= -0.4545 in CFM, PFM, and PFM-Fe respectively) attached to it. Iron atom (Fe46 = 0.7185) has a high positive charge showing electropositive character.

The electrostatic potential surfaces are correlated with the charge density, shape, dipole moment, and position of chemical reactivity of the molecules. As inspected from the MEPs map of the title compounds (Fig. 10), the negative regions are localized over the electronegative oxygen and nitrogen atoms. The maximum positive regions are localized on the hydrogen atoms and the metal ion [25].

3.6.3 Molecular reactivity

The electron donor-acceptor properties of various types of molecules can be defined by using the energy of HOMO and LUMO. FMO's also helped to interpret the kinetic stability, charge transfer, and chemical reactivity of a molecule. The frontier molecular orbital distribution of the compounds CFM, PFM, and PFM-Fe were represented in Fig. 11a. The smaller value of the HOMO and LUMO energy gap showed that the studied molecule has high polarizability, chemical reactivity, and biological activity.

In the PFM molecule, the HOMO (−6.621 eV) and the LUMO (−2.506 eV) are situated at the benzene and pyrazoline ring, respectively. For the PFM-Fe, the electron density of HOMO (−16.079 eV) is mainly situated at the molecular framework. Whereas, the electron density of LUMO (−14.062 eV) is situated at the coordination center. The calculated energy gap (Δ) between HOMO and LUMO for PFM-Fe is found to be 2.02 eV, which is lower than that of unbound PFM (4.12 eV). Based on the DFT calculations, the binding between PFM and Fe is energetically favorable. These DFT results implied that the interaction of Fe to PFM effectively decreases the HOMO−LUMO energy gap of the PFM-Fe and intensely stabilizes the sensing of Fe by forming PFM-Fe compound [26]. Furthermore, the chemical reactivity parameters of the compounds (Table 2) were also calculated with the help of the energy of HOMO and LUMO orbitals. Using FMOs energies, the ionization potential (I) and electron affinity (A) can be measured as: $I = -E_{HOMO}$ and $A = -E_{LUMO}$.

Table 2
Chemical Reactivity Parameters of the Compounds Based on HOMO-LUMO

S. No.	CFM	PFM	PFM-FE
E_{HOMO} (eV)	-7.308	-6.6216	-16.0792
E_{LUMO} (eV)	-2.133	-2.5064	-14.0623
$\Delta E_{HOMO-LUMO}$ (eV)	5.1747	4.11517	2.0169
Ionization potential (IP) (eV)	7.308	6.6216	16.0792
Electron affinity(EA) (eV)	2.133	2.5064	14.0623
Chemical potential (eV)	-4.7207	-4.564	-15.07076
Electronegativity(eV)	4.7207	4.564	15.07076
Chemical hardness (eV)	2.5873	2.0575	1.008454
Chemical Softness $(eV)^{-1}$	0.1932	0.243	0.495808
Electrophilic global index (eV)	4.3065	5.0618	112.611

Moreover, Density of States (DOS) plots of PFM are examined to study the electronic structure of the molecule via population analysis of orbitals. DOS plot represents the energy level of each orbital. DOS plot (Fig. 11b) for PFM shows that FMOs and the energy gap of HOMO-LUMO are in complete agreement with the result obtained from the DFT study [27]. To investigate the optimization process Figure S12a, a graph displaying deviation from the target was plotted (Figure S12b). Also, the graph energy vs. optimization step was plotted as shown in Figure S12c. In these plots, the path of structure convergence was established. As inspected from these plots, the self-consistent field is converging as the line is directed towards zero [28].

Note

Some other important thermodynamics parameters, NBO, Vibrational analysis, and NMR of the compounds based on theoretical results are discussed in section 1 of the SI.

3.7 Detection of Fe^{3+} in water samples

The synthesized PFM sensor was utilized for the detection of Fe^{3+} in different water samples (river water, tap water, and sewage waste water) by using the spike recovery method. All the samples were spiked with different concentrations of Fe^{3+} and the results obtained were shown in Table 3. It can be seen that the detected Fe^{3+} ions concentration is close to the spiked value with a satisfactory recovery values (99.0–101.0%) and low RSD values (0.78–2.03%). This signifies the great practical potential of the present method for the detection of Fe^{3+} in water samples.

Table 3
Detection of Fe3+ in different water samples (tap, river, and sewage waste water) by the proposed PFM sensor

Order	Matrix	Amount spiked (μM)	Amount found (μM)	Recovery %	RSD %
1	River water	0.89	0.878	98.6	0.85
		1.79	1.77	98.8	0.91
		2.50	2.43	97.2	0.78
2	Tap water	0.89	0.884	99.3	1.23
		1.79	1.79	100.0	1.11
		2.50	2.48	99.2	2.03
3	Sewage waste water	0.89	0.88	98.8	0.59
		1.79	1.79	100.0	0.96
		2.50	2.50	100.0	1.20

3.8 Comparison with other reported Fe^{3+} Fluorescent sensors

To provide quantifiable achievement for the design of a new fluorescent sensor, the sensing performance of PFM was compared with some reported pyrazoline based fluorescent sensors for Fe^{3+} detection (Table 4). As shown in Table 4, the synthesized fluorescent ligand PFM showed a better detection limit for Fe^{3+} (0.12 μM) in comparison to other reported sensors. Pyrazoline based fluorescent sensors such as P [29], Q [30], R [31], and S [32] showed good selectivity for Fe^{3+} ions, but were not used for any real sample analysis. Pyrazole-pyrazoline based sensor (U) [33] showed a better detection limit but the synthetic process was tedious and involved 4 step reaction. On the other hand, the present procedure involves a simple procedure with 2 step reaction (Scheme 1). Moreover, the sensor showed better extraction recovery of 99–101% (tap, river, and sewage waste water) with RSD < 2.1% than the other reported methods.

Table 4
Comparison of sensor PFM with other sensor for detection of iron(III).

Order	Fluorescent chemosensor	Linear range (μM)	Detection limit (μM)	Recovery %	R.S.D %	Matrix	Ref
1	2-(5-(4-Chlorophenyl)-3-(pyridin-2-yl)-4,5-dihydropyrazol-1-yl) 4 benzo[d]thiazole (P)	10–200	3.0				[29]
2	3-(2,5-dimethylthiophen-3-yl)-5-(9-ethyl-9H-carbazol-3-yl)-4,5- dihydro-1H-pyrazol-1-yl)benzo[d]thiazole(Q)	10–90					[30]
3	2-(1-(benzo[d]thiazol-2-yl)-5-(3,4-dimethoxyphenyl)-4,5-dihydro-1Hpyrazol-3-yl)phenol(R)	10–50					[31]
4	(2-(3-(pyridin-2-yl)-5-(3,4,5-trimethoxyphenyl)-4,5-dihydro-1H-pyrazol-1-yl)benzo[d]thiazole) (S)	0–40					[32]
5	4-(2-(3-Methyl-5-oxo-1-tosyl-1H-pyrazol-4(5H)-ylidene)hydrazinyl)-N-(pyrimidin-2-yl)benzenesulfonamide (T)	20–100	17	94.8–97	1.3–2.34	River, ground, and tap water	[4]
6	coumarin-based pyrazoline	0–120	0.101			Imaging in HeLa cells	[34]
7	Pyrazole-pyrazoline (U)	0–10	.00039				[33]
8	5-(4-methoxyphenyl)-3-(5-methylfuran-2-yl)-1-phenyl-4,5-dihydro-1*H*-pyrazole (PFM)	0–3	0.12	97.2–100	0.59–2.03	Tap, river and sewage waste water	**This work**

4. Conclusions

The synthesized organic fluorescent probe based on pyrazoline 5-(4-methoxyphenyl)-3-(5-methylfuran-2-yl)-1-phenyl-4, 5-dihydro-1*H*-pyrazole **(**PFM**)** has been designed for the selective detection of Fe^{3+} ions. The sensor PFM displayed a “turn off” fluorescence response towards Fe^{3+} ion with a detection limit of

0.12 μM. The binding stoichiometry of Fe^{3+} ions with PFM was 1:1 confirmed by Job's plot, and their binding mechanism of them was demonstrated by paramagnetic enhanced quenching, FRET and density functional theory (DFT) study. The proposed PFM-sensor was satisfactory applied for quantitative and cost- effective detection of Fe^{3+} with good precision in real samples.

Declarations

Acknowledgement

The authors (PS, SB, IM, MY, and AKM) acknowledge the UGC-SAP and Chemistry Department, Punjabi University, Patiala, for providing lab and instrument facilities. AKM is also thankful to the UGC, New Delhi for the award of Mid-Career award to him.

Authors' Contributions Promila Sharma: Performed the experimentation. Shikha Bhogal, Irshad Mohiuddin: Helped in performing the experiments. Mohammad Yusuf and Ashok Kumar Malik: Helped in writing and supervised the research work.

Funding The authors did not receive support from any organization for the submitted work and have no financial or non- financial interests to disclose.

Availability of Data and Material Data and material information is provided and will be shared on request.

Ethics Approval There are no ethic approvals required for this research work.

Consent to Participate All authors will participate in the revision of the manuscript.

Consent for Publication All authors agree for the publication.

Conflicts of Interest/Competing Interests All the authors declare that there is no conflict of interest.

References

1. Chung, P.K., et al., *A pyrene-based highly selective turn-on fluorescent chemosensor for iron (iii) ions and its application in living cell imaging.* Journal of fluorescence, 2013. **23**(6): p. 1139-1145.
2. Maity, P., et al., *Highly selective and sensitive benzo-imidazo-pyrrolo [3, 4-c] pyridines based chemosensor for iron, DFT calculation and its biological application.* Journal of Molecular Structure, 2021. **1236**: p. 130280.
3. Li, C., et al., *Reaction-based highly selective and sensitive monomer/polymer probes with Schiff base groups for the detection of Hg2+ and Fe3+ ions.* Spectrochimica Acta Part A: Molecular and Biomolecular Spectroscopy, 2020. **243**: p. 118763.
4. Sayed, A., et al., *A novel fluorescent sensor for fast and highly selective turn-off detection of Fe3+ in water and pharmaceutical samples using synthesized azopyrazole-benzenesulfonamide derivative.*

Journal of Molecular Structure, 2021. **1225**: p. 129175.

5. Wang, M., L. Guo, and D. Cao, *Porous organic polymer nanotubes as luminescent probe for highly selective and sensitive detection of Fe 3+.* Science China Chemistry, 2017. **60**(8): p. 1090-1097.
6. Vanjare, B.D., et al., *Discriminating chemosensor for detection of Fe3+ in aqueous media by fluorescence quenching methodology.* Bulletin of the Korean Chemical Society, 2018. **39**(5): p. 631-637.
7. Zhang, B., et al., *A dual-response quinoline-based fluorescent sensor for the detection of Copper (II) and Iron (III) ions in aqueous medium.* Sensors and Actuators B: Chemical, 2017. **243**: p. 765-774.
8. Zhang, Y.-P., et al., *Fluorogenic recognition of Zn2+, Cd2+ by a new Pyrazoline-based Multi-Analyte chemosensor and its application in live cell imaging.* Inorganic Chemistry Communications, 2021. **130**: p. 108735.
9. Zhang, L., et al., *High solid fluorescence of a pyrazoline derivative through hydrogen bonding.* Molecules, 2017. **22**(8): p. 1304.
10. Varghese, B., et al., *Unveiling a versatile heterocycle: pyrazoline–a review.* RSC advances, 2017. **7**(74): p. 46999-47016.
11. Shaaban, M.R., A.S. Mayhoub, and A.M. Farag, *Recent advances in the therapeutic applications of pyrazolines.* Expert opinion on therapeutic patents, 2012. **22**(3): p. 253-291.
12. Singh, P., et al., *2-Pyrazolines as biologically active and fluorescent agents, an overview.* Anti-Cancer Agents in Medicinal Chemistry (Formerly Current Medicinal Chemistry-Anti-Cancer Agents), 2018. **18**(10): p. 1366-1385.
13. Hasan, A., A. Abbas, and M.N. Akhtar, *Synthesis, characterization and fluorescent property evaluation of 1, 3, 5-triaryl-2-pyrazolines.* Molecules, 2011. **16**(9): p. 7789-7802.
14. Sharma, P., et al., *Experimental and Theoretical Studies of the Pyrazoline Derivative 5-(4-methylphenyl)-3-(5-methylfuran-2-yl)-1-phenyl-4, 5-dihydro-1H-Pyrazole and its Application for Selective Detection of Cd2+ ion as Fluorescent Sensor.* Journal of Fluorescence, 2022: p. 1-13.
15. Bhogal, S., et al., *Synchronous Fluorescence Determination of Al3+ Using 3-Hydroxy-2-(4-Methoxy Phenyl)-4H-Chromen-4-One as a Fluorescent Probe.* Journal of Fluorescence, 2021: p. 1-9.
16. Holla, B.S., P. Akberali, and M. Shivananda, *Studies on arylfuran derivatives: Part X. Synthesis and antibacterial properties of arylfuryl-Δ2-pyrazolines.* Il Farmaco, 2000. **55**(4): p. 256-263.
17. Han, C., et al., *Design and synthesis of a highly sensitive "Turn-On" fluorescent organic nanoprobe for iron (iii) detection and imaging.* Journal of Materials Chemistry C, 2014. **2**(43): p. 9077-9082.
18. Joshi, S., et al., *Experimental and theoretical study: Determination of dipole moment of synthesized coumarin–triazole derivatives and application as turn off fluorescence sensor: High sensitivity for iron (III) ions.* Sensors and Actuators B: Chemical, 2015. **220**: p. 1266-1278.
19. Rahaman, S., et al., *Synthesis and antihistaminic activity of novel pyrazoline derivatives.* International Journal of Chem Tech Research, 2010. **2**: p. 16-20.

20. Nisa, S. and M. Yusuf, *Synthetic and antimicrobial studies of N-substituted-pyrazoline-based new bisheterocycles.* Journal of Heterocyclic Chemistry, 2020. **57**(4): p. 2024-2036.
21. Kumar, M., et al., *A selective 'turn-on'fluorescent chemosensor for detection of Al3+ in aqueous medium: experimental and theoretical studies.* Sensors and Actuators B: Chemical, 2018. **260**: p. 888-899.
22. Udhayakumari, D., et al., *Highly fluorescent probe for copper (II) ion based on commercially available compounds and live cell imaging.* Sensors and Actuators B: Chemical, 2014. **198**: p. 285-293.
23. Saravanamoorthy, S., B. Vasanthi, and R. Poornima, *Molecular Geometry, Vibrational Spectroscopic, Molecular Orbital and Mulliken Charge Analysis of 4-(Carboxyamino)-Benzoic Acid: Molecular Docking and Dft Calculations.* 2021.
24. Subashini, G., et al., *Quinoline appended pyrazoline based Ni sensor and its application towards live cell imaging and environmental monitoring.* Sensors and Actuators B: Chemical, 2017. **243**: p. 549-556.
25. Issa, T.B., et al., *Synthesis, crystal structure, DFT calculations and molecular docking of L-pyroglutamic acid.* Journal of Molecular Structure, 2019. **1178**: p. 436-449.
26. Zuo, Z., et al., *A dual responsive colorimetric/fluorescent turn-on sensor for highly selective, sensitive and fast detection of Fe3+ ions and its applications.* Journal of Photochemistry and Photobiology A: Chemistry, 2019. **382**: p. 111876.
27. Muthu, S. and E.I. Paulraj, *Molecular structure and spectroscopic characterization of ethyl 4-aminobenzoate with experimental techniques and DFT quantum chemical calculations.* Spectrochimica Acta Part A: Molecular and Biomolecular Spectroscopy, 2013. **112**: p. 169-181.
28. Berhanu, A.L., et al., *Experimental and theoretical studies of the schiff base (Z)-1-(thiophen-2-yl-methyleneamino) propane-2-ol.* Journal of Molecular Structure, 2020. **1200**: p. 127104.
29. Hu, S., et al., *A new selective fluorescent sensor for Fe3+ based on a pyrazoline derivative.* Spectrochimica Acta Part A: Molecular and Biomolecular Spectroscopy, 2013. **113**: p. 325-331.
30. Asiri, A.M., et al., *Physicochemical and Photophysical investigation of newly synthesized carbazole containing pyrazoline-benzothiazole as fluorescent chemosensor for the detection of Cu2+, Fe3+ & Fe2+ metal ion.* Journal of Molecular Structure, 2019. **1195**: p. 670-680.
31. Khan, S.A., *Multi-step synthesis, photophysical and physicochemical investigation of novel pyrazoline a heterocyclic D-π-A chromophore as a fluorescent chemosensor for the detection of Fe3+ metal ion.* Journal of Molecular Structure, 2020. **1211**: p. 128084.
32. Asiri, A.M., M.M. Al-Amari, and S.A. Khan, *Multistep Synthesis and Photophysical Investigation of Novel Pyrazoline, a Heterocyclic D-π-a Chromophore (PTPB) as a Fluorescent Chemosensor for the Detection of Fe3+ Metal Ion.* Polycyclic Aromatic Compounds, 2020: p. 1-15.
33. Zhang, Y.-P., et al., *A novel fluorescent probe based on pyrazole-pyrazoline for Fe (III) ions recognition.* Journal of Fluorescence, 2021. **31**(1): p. 29-38.
34. Zhang, Y.-P., et al., *A novel coumarin-based pyrazoline fluorescent probe for detection of Fe3+ and its application in cells.* Inorganica Chimica Acta, 2021. **525**: p. 120469.

Scheme

Scheme 1 is available in the Supplementary Files section.

Figures

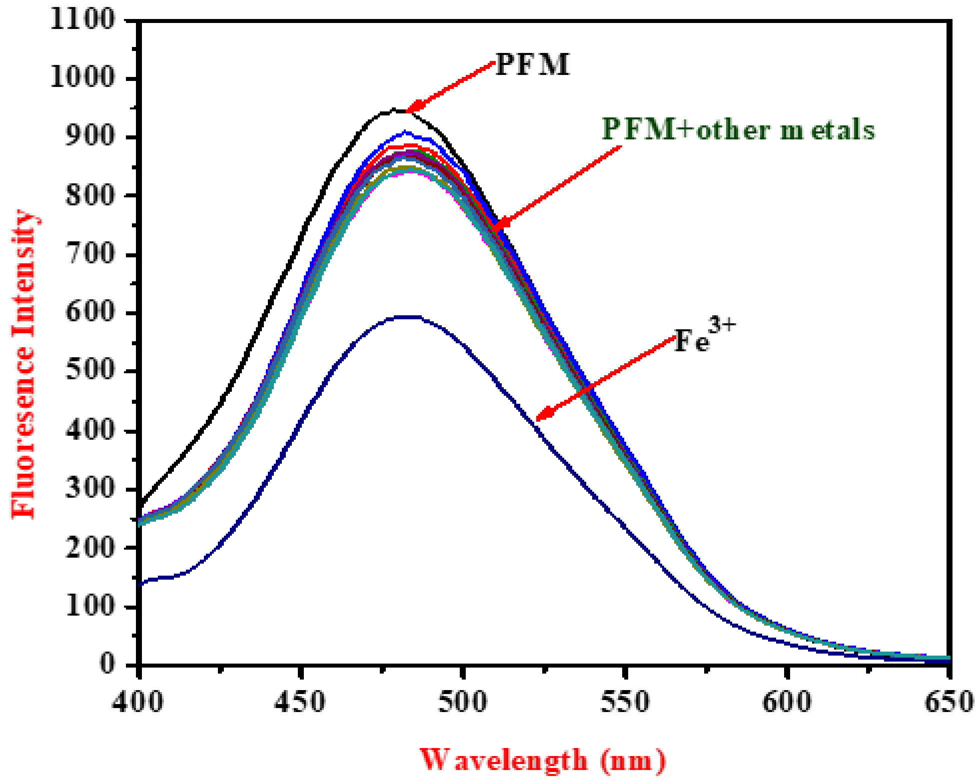

Figure 1

Fluorescence spectra of PFM (2 x 10^{-5} M) in methanol:water (1:9) upon addition of various metal ions (1μM) (Ex. Wavelength 350 nm).

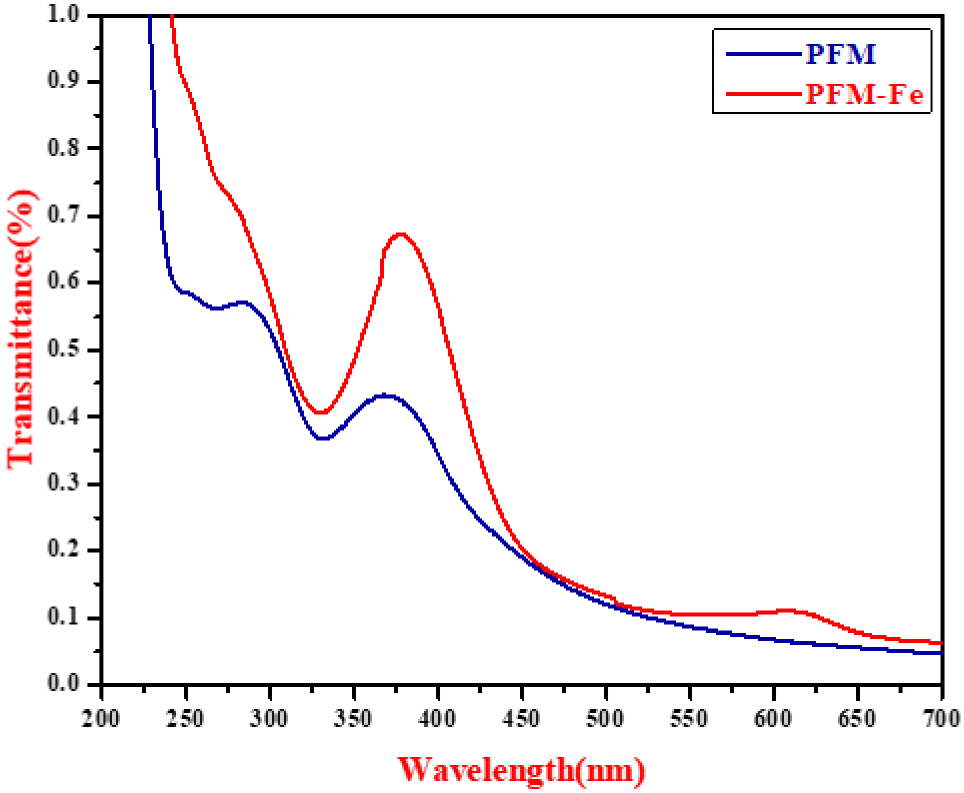

Figure 2

UV-Vis spectrum of PFM and PFM-Fe.

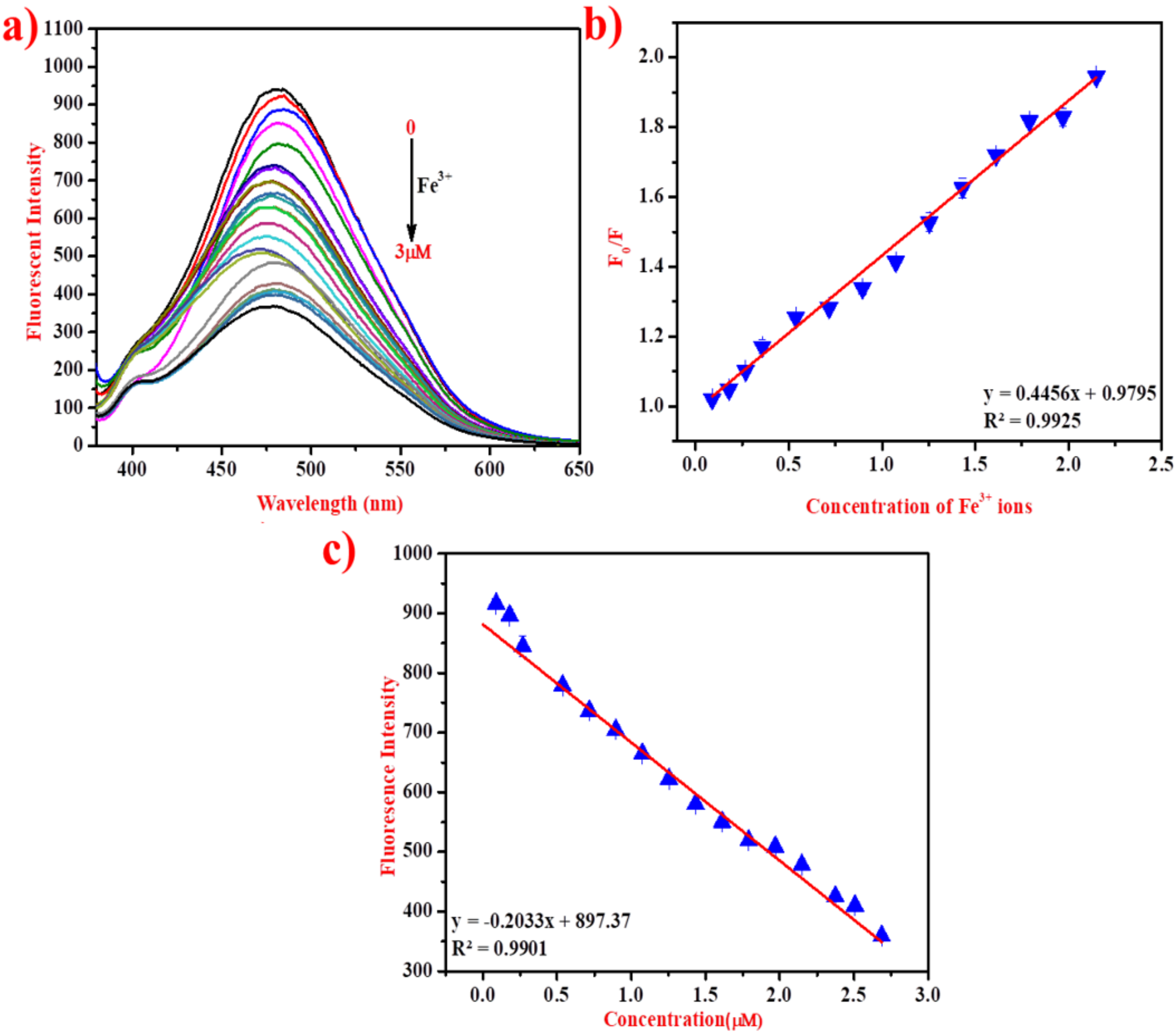

Figure 3

a) Fluorescence spectra of PFM with increasing concentration of Fe^{3+} ions **b)** Stern-Volmer plot for PFM against varying concentrations of iron ions in the range of 0-3 μM **c)** Calibration curve of fluorescence intensity of PFM at 484 nm vs. concentration of iron ion excited at 350 nm.

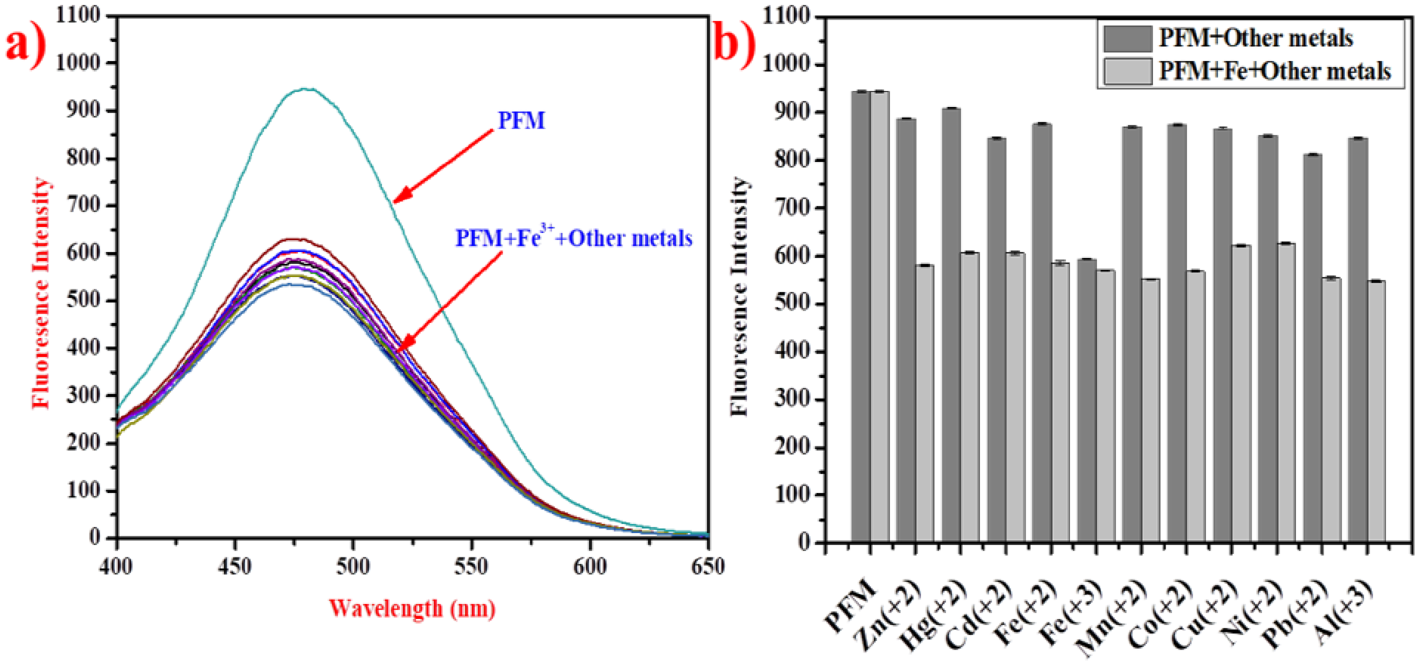

Figure 4

a) Fluorescence response of PFM upon addition of Fe^{3+} ion in the presence of other competing metal ions (Ex. Wavelength 350nm) **b)** Dark grey bars represent the fluorescence intensity of PFM in the presence of 1μM of metal ion. light grey bars represent the fluorescence intensity in the presence of various metal ions after the addition of Fe^{3+}.

Figure 5

Job's plot for determining the stoichiometry for PFM and Fe^{3+} ions

Figure 6

Benesi–Hildebrand plot (at 350 nm) for complexation of PFM with Fe^{3+} ion.

Figure 7

Proposed binding modes of PFM with Fe^{3+} ions.

Figure 8

Optimized geometric structures of CFM, PFM, and PFM-Fe at B3LYP/6-311G (d,p).

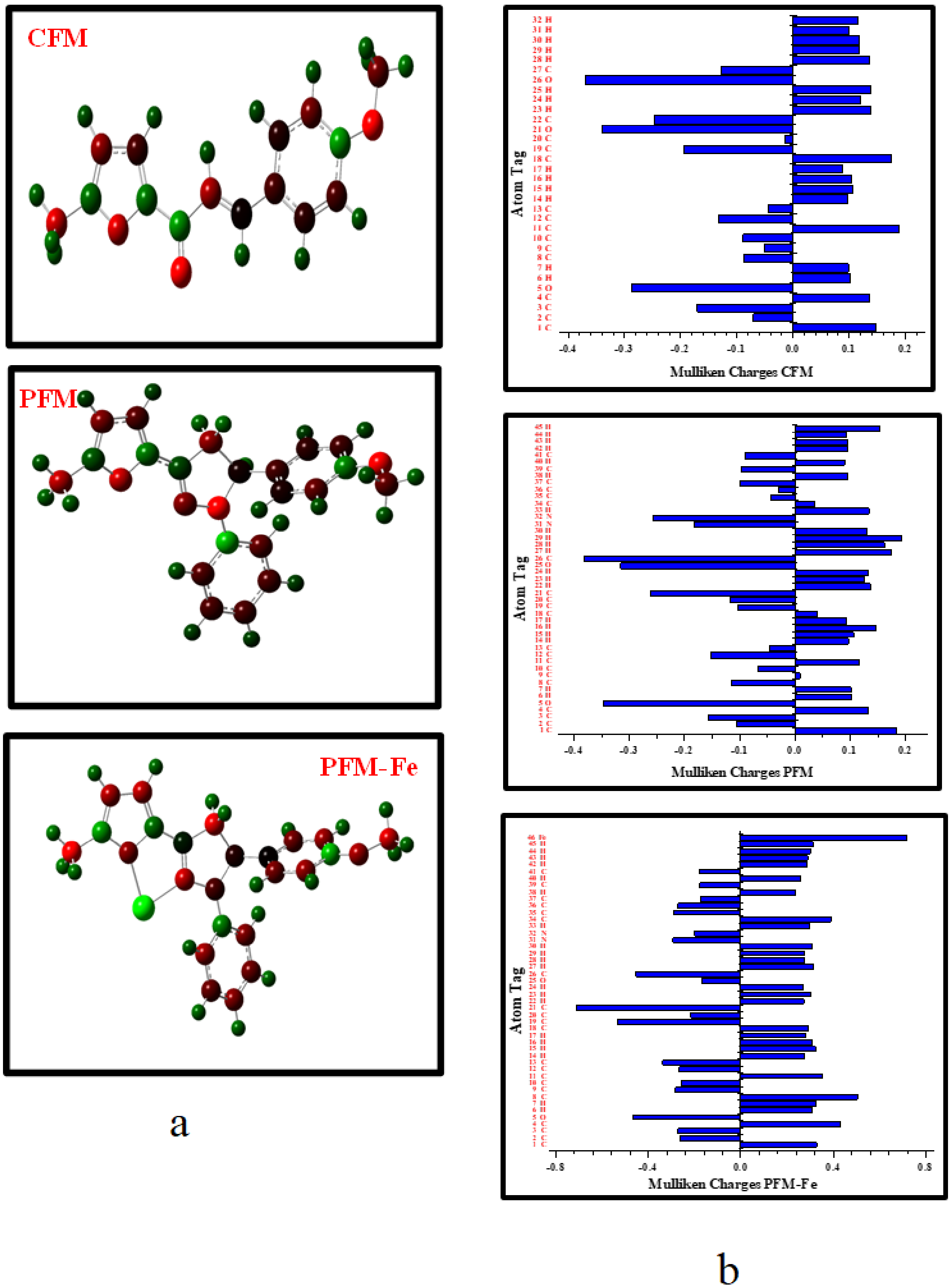

Figure 9

a: Mulliken charges of CFM, PFM, and PFM-Fe at B3LYP/6-311G (d,p).

b: Horizontal bar diagram of mulliken atomic charges of title compounds at B3LYP/6-311G(d,p).

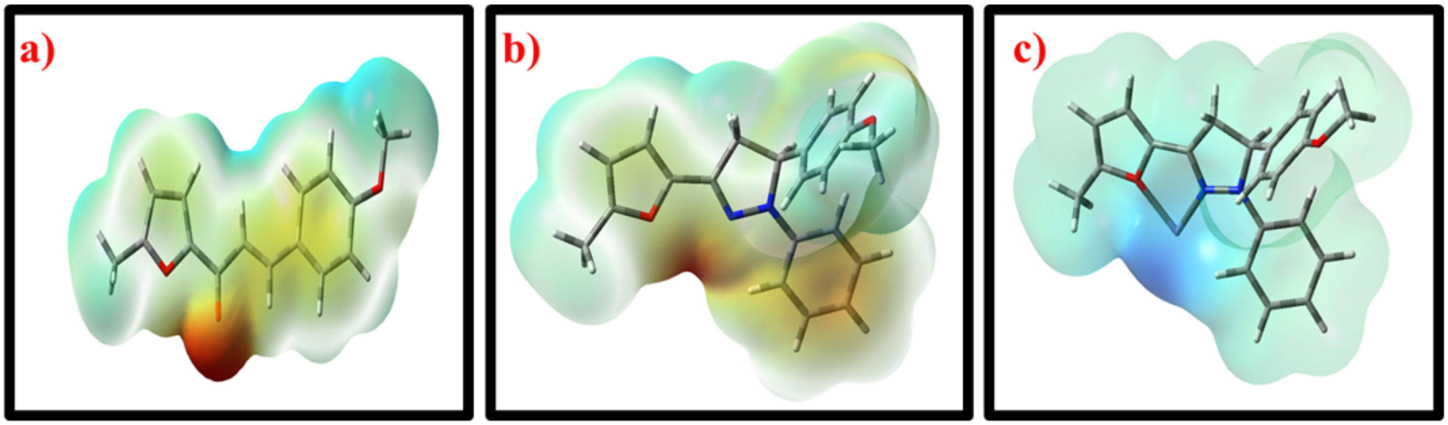

Figure 10

Molecular electrostatic potential (MEPs) of compounds of CFM, PFM, and PFM-Fe at B3LYP/6-311G (d,p) (most electronegative electrostatic potential are red, most positive electrostatic potential are blue and t regions close to zero potential are green).

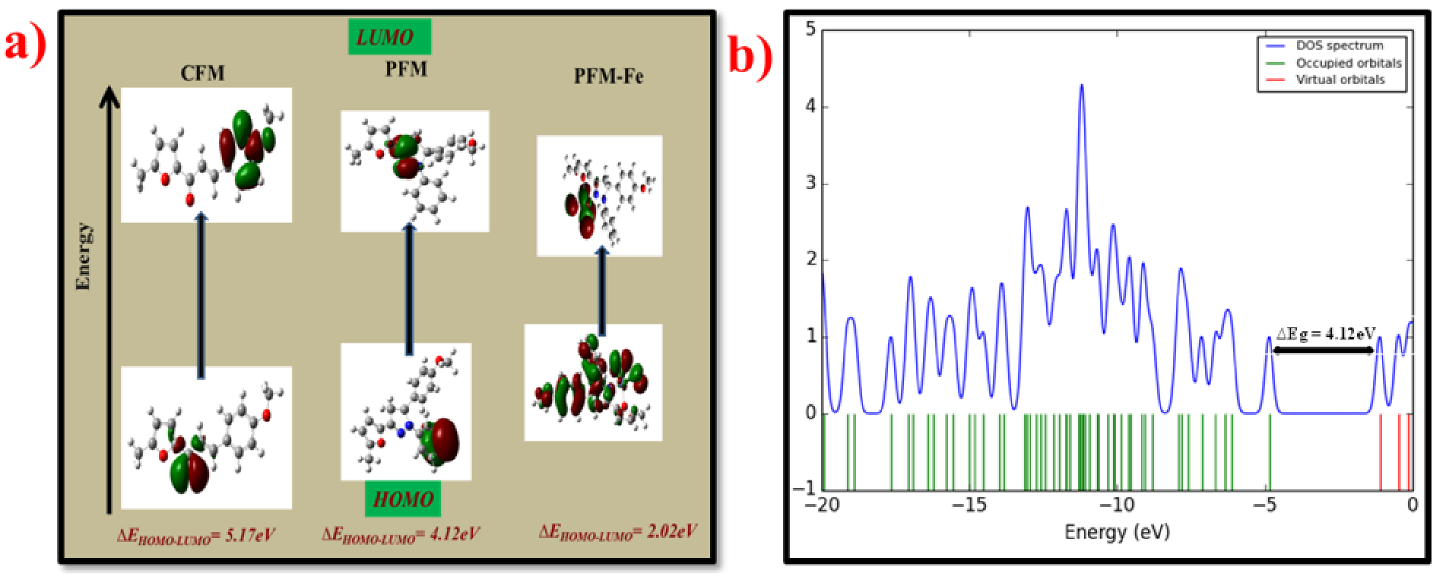

Figure 11

a) FMOs of compounds of CFM, PFM, and PFM-Fe at B3LYP/6-311G (d,p)

b) Calculated TDOS diagram of PFM using gaussum software.

Supplementary Files

This is a list of supplementary files associated with this preprint. Click to download.

- 220615SIPFMFeV2PS.docx
- Scheme.png